Can we describe graphene confined water structures as overlapping of approaching graphene-water interfacial structures?

Journal:	*The Journal of Physical Chemistry*
Manuscript ID	Draft
Manuscript Type:	Article
Date Submitted by the Author:	n/a
Complete List of Authors:	Chialvo, Ariel; Oak Ridge National Laboratory, Chemical Sciences Division Vlcek, Lukas; Oak Ridge National Laboratory, Chemical Sciences Division; Oak Ridge National Laboratory, Joint Institute for Computational Sciences

Can we describe graphene confined water structures as overlapping of approaching graphene-water interfacial structures?

Ariel A. Chialvo[1] and Lukas Vlcek[1,2,&]

[1] Chemical Sciences Division, Geochemistry & Interfacial Sciences Group
Oak Ridge National Laboratory, Oak Ridge, TN 37831-6110, U. S. A.

[2] Joint Institute for Computational Sciences
Oak Ridge National Laboratory, Oak Ridge, TN 37831-6173, U. S. A.

[&] To whom correspondence should be addressed (vlcekl1@ornl.gov, FAX 865-574-4961)

December 4, 2015

ABSTRACT

We investigate the microscopic mechanisms of the overlap of interfacial structures in confined fluids and attempt to answer the question whether the confined structures can be predicted from the original density profiles of individual solid-fluid interfaces. For that purpose we perform (globally) isobaric-isothermal (locally, grand canonical) molecular dynamics simulations to extract not only the axial distribution functions of the water-sites for the uncoupled graphene-water interfaces, but also those corresponding to the confined aqueous environments over the interplate range $8 \le h(\mathring{A}) \le 28$ typically at ambient conditions. We have tested two (*i.e.*, an arithmetic and a geometric) superposition approximations for the singlet density of confined water between flat graphene plates, as well as for a combination of flat and corrugated graphene plates. The outcome of this study suggests that the answer to the title's question is a "yes", provided that the interplate distance h is large enough to avoid fluid geometric packing frustration.

I. INTRODUCTION

Water confinement between solid surfaces has been the focus of intense research aimed at unraveling the microscopic behavior of water at solid-water interfaces including theoretical developments [1-4], experimental techniques [5-10], and molecular simulation approaches [11-25]. The outcome of these studies have indicated *inter alia* that solid-fluid interfaces typically induce significant changes in the microstructure (*e.g.*, stratification), dynamics (*e.g.*, slow down), and response functions (*e.g.*, enhancement) of water [26-30]; a behavior ascribed to the clear interaction asymmetry between the fluid-fluid and surface-surface interactions, resulting from the presence of the solid surface and translating into inhomogeneous density (and consequent fluid property) distributions. These inhomogeneous distributions usually exhibit oscillatory decay to their corresponding bulk values, with a periodicity commensurate with the fluid molecular diameter, and usually within a few molecular diameters from the interface [19, 31-37], unless they encounter and overlap with other inhomogeneous regions, *i.e.*, with the consequent formation of confined environments [38-40].

Obviously, the experimentally observed and molecular-based simulated water density profiles (*i.e.*, singlet axial distributions) depend not only on the type of solid substrate [41-47] but also on the topography of the solid surface [48-54], *i.e.*, on the surface wettability resulting from the hydrophilic-hydrophobic nature of the fluid-substrate interactions. Recent advances in the experimental determination of the structure factor of fluids under confinement [55-58] have put in the spotlight the need for an improved understanding of the behavior of anisotropic pair distribution functions and their link with the corresponding singlet distributions concerning purely interfacial as well as confined aqueous environments. Moreover, the value of the interfacial data from x-ray reflectivity (XRR), [36] neutron reflectivity (NR), and surface force apparatus (SFA) [59-60] can be greatly magnified if they can be translated into density profiles for the eventual confined environment counterpart, as predictions for the overlapping of interfacial structures or as tests of accuracy of the approximations underlying the interpretation of raw data from confined fluid XRR experiments [35, 56].

In this context the question we would like to address here regards the microscopic understanding of such an overlapping process and whether the resulting inhomogeneous

density profile of the confined polar fluid can be described in terms of the original inhomogeneous density profiles near the solid-fluid interfaces under the same fluid chemical potential at the prevailing fixed state conditions of temperature and pressure (see Figure 1). For that purpose, in section II, we introduce some essential statistical mechanics background and discuss the ideas behind the test of several approximations to represent the actual inhomogeneous density distribution of water under graphene plate confinement. In section III we briefly describe the atomistic models and the molecular-based simulation method underlying the determination of the microstructural information in terms of water-site axial density profiles and normalized singlet distribution functions. Then in section IV we discuss the resulting simulated density profiles in the context of the two superposition approaches, and close the paper in with a summary of the most relevant findings in section V where highlight the realism and limitations of the superposition approximations to describe the actual axial density profiles of the water sites in graphene confined aqueous systems.

II. FUNDAMENTALS

The knowledge of the density profile $\rho(z)$ of a fluid as a function of distance z from a solid surface provides essential information to build the thermodynamics of the solid-fluid interfacial system, in particular, the so-called surface adsorption excess, *i.e.,*

$$\begin{aligned}\Gamma &= \int_0^h \left[\rho(z)-\rho_b\right]dz \\ &= \int_0^{0.5h}\left[\rho(z)-\rho_b\right]dz + \int_{0.5h}^{h}\left[\rho(h-z)-\rho_b\right]dz\end{aligned} \tag{1}$$

where $\rho_b = \rho(h \to large, T, \mu)$ denotes the bulk density, $\rho(z) = \rho(h-z)$ represents the "left-confined" and "right-confined" fluid density profiles, and "large" means a few fluid's molecular diameters. Moreover, note the limiting condition of Eqn. (1), *i.e.*,

$$\lim_{h\to large} \Gamma = \Gamma_{left} + \Gamma_{right} \ . \tag{2}$$

If the *left* and *right* interfaces are identical, the total adsorption excess is simply the double of that for the free-standing interfaces. In this case Eqn. (2) highlights the fact that the solid-fluid interfacial structures of the left- and right-plates become identical as soon

as the fluid local density $\rho(0.5h) \cong \rho_b$ and stays the same for larger inter-plate distance h, *i.e.*, the interfacial structures become uncoupled. This condition poses a logical follow-up question of whether it is possible to estimate the inhomogeneous density profiles of confined fluids from individual density profiles of free-standing solid-fluid interfaces even for considerably shorter distance between the interfaces, *i.e.*,

$$\rho_{conf}(z) \stackrel{?}{=} \mathcal{F}\left[\rho_{left}(z), \rho_{right}(h-z)\right] \tag{3}$$

where $\mathcal{F}\left[\cdots\right]$ represents a potential functional connection between the interfacial density profiles of the free-standing plates and the confined counterparts resulting from the overlapping of two approaching solid-fluid interfacial structures as illustrated in Figure 1.

Physically motivated approximations underlying the general relation in Eqn. (3) can be derived by considering the basic factors influencing the density distribution of fluids in external potentials. Given the nature of the systems under consideration, the confined water environment can be described in terms of the grand canonical ensemble, *i.e.*, according to the grand potential $\Omega = U - TS - \mu N$ where U, S, and μ are the internal energy, entropy and chemical potential characterizing the system comprising N fluid particles at the temperature T [61]. Moreover, considering that the solid surfaces behave as an external potential $\Phi_{ext}(z) = \Phi_{left}(z) + \Phi_{right}(h-z)$, where $\Phi_{\alpha}(\cdots)$ represents the $\alpha-$plate /fluid interaction potential in the $z-$direction and h is the interplate distance, the resulting inhomogeneous density distribution becomes defined by the functional differentiation of the grand partition function [62], *i.e.*,

$$\delta\Omega / \delta\phi(z) \equiv -\rho(z) \tag{4}$$

with $\phi(z) = \mu - \Phi_{ext}(z)$, where the chemical potential μ of the fluid confined in external potential $\Phi_{ext}(z)$ is uniform across the system and equal to that of the bulk fluid at the same thermodynamic conditions,[63] *i.e.*,

$$\mu = kT \ln\left[\rho_b \Lambda^3\right] - kTc_b^{(1)} = kT \ln\left[\rho(z)\Lambda^3\right] + \Phi_{ext}(z) - kTc^{(1)}(z) \tag{5}$$

Here $\Lambda = \sqrt{h^2\beta/2m\pi}$ is the thermal de Broglie wavelength, $\beta = 1/kT$, and $c^{(1)}(z)$ represents the one-particle direct correlation function. For unconfined (bulk) system the direct correlation function is constant and proportional to the excess chemical potential, $-kTc_b^{(1)} = \mu_b^{ex}$, and in confined systems it is determined purely by fluid-fluid interactions, which can be considered as resulting in an effective position-dependent potential $\omega(z) = -kTc^{(1)}(z)$. Accordingly, Eqn. (5) can be re-written for the confined fluid density profile as follows,

$$\rho(z) = \rho_b \exp\left[\beta\mu_b^{ex} - \beta\{\Phi_{ext}(z) + \omega(z)\}\right] = \rho_b \exp\left[-\beta w(z)\right] \qquad (6)$$

PMF

where $w(z)$ is the total potential of mean force acting on the fluid molecules. For the purpose of this article we will assume that the external potential $\Phi_{ext}(z)$ is unknown (as in experimental systems) and we want to predict $\rho(z)$ of the confined fluid only from the knowledge of the individual interfacial profiles and from the known thermodynamic properties of the bulk fluid. The only assumption we have on the external potential is that the contributions from the two opposing surfaces are additive, as suggested earlier.

Possibly the simplest approximation allowing us to estimate the confined fluid profiles is to assume that the total potential of mean force is additive in the same way as the external potentials, *i.e.*, $w(z) = w_{left}(z) + w_{right}(h-z)$. Defining the axial distribution function as $g(z) = \rho(z)/\rho_b(z)$, the additivity of $w(z)$ leads to the *geometric* superposition approximation, *i.e.*,

correct here

$$g_{conf}(z) = \exp\left[-\beta\{w_{left}(z) + w_{right}(h-z)\}\right] = g_{left}(z) \times g_{right}(h-z) \qquad (7)$$

For small external potential perturbations leading to small potentials of mean force, the exponential in Eqn. (7) can be written as a series expansion and, after retaining the first-order term, the axial distribution function of the confined fluid can be written as follows,

$$g_{conf}(z) \approx 1 - \beta w_{left}(z) - \beta w_{right}(h-z) \approx g_{left}(z) + g_{right}(h-z) - 1 \qquad (8)$$

This approximation can be expected to perform reasonably well only for very small perturbations, such as in the case of relatively distant confining surfaces. It is easy to see that combining large density fluctuations that are present near the solid-fluid contact according to Eqn. (8) may lead to unphysical predictions of negative fluid densities.

The *arithmetic* superposition in Eqn. (8) bears some similarity with the approximation underlying the electronic density profiles in the general density functional formalism for electron gases [64-65], in particular its first order approximation according to a statistical perturbation approach, *i.e*., Eqn. (3) of Gombás [66] and Eqn. (2) of Gaydaenko and Nikulin [67]. Moreover, the description of the PMF profile involving the *geometric* superposition in Eqn. (7) is a particular variant of Kirkwood's original superposition approximation [68] and becomes equivalent to the first order approximation introduced by Verwey and Overbeek [69] to describe the electric potential of an electrolyte between two parallel flat plates as the overlapping of two non-interacting electric double layers (see Eqns. 32-33 of Verwey and Overbeek). These are encouraging signs on the plausible realism of the representations embedded in the approximation given by Eqns. (7)-(8).

While the preceding relations are simple and practical, it should be born in mind that they are limited by the assumption of additivity of the total potential of mean force. According to the examples given in the following section the proposed relations are reasonable for the investigated cases, yet we should cautious when applying them to the cases of extreme confinement accommodating only a single layer, in which crystal-like structuring may occur and the assumption of the overlap of two fluid-solid interfaces may not be fully justified.

III. MODELS AND SIMULATION METHODOLOGY

The approximate relations introduced in the previous section were tested by means of isobaric-isothermal molecular dynamics simulations. The simulated system comprised 2048 water molecules described by the SPC/E water model [70] and the thermodynamic condition T=298K and P=1atm were maintained using our own implementation of a Nosé-Poincare symplectic integration algorithm [71-72] with a 2.0fs time-step size. The tetragonal simulation box with dimensions $\mathbb{L}_z = 2\mathbb{L}_x = 2\mathbb{L}_y$, and subject to 3D periodic boundary conditions, contained two immersed identical (in

registry) graphene plates, with dimensions $L_x = 18.74 Å$ by $L_y = 20.28 Å$, approximately equidistant from the center of the box while kept fixed in space and separated by an interplate distance $8 \le h(Å) \le 28$ during the simulation. All simulations comprised 20 ns of phase space trajectory after a 0.5ns re-equilibration from previous runs involving similar state conditions, interplate separations, or plate configurations. add here the equilibration statement

Each graphene plate comprised 136 atomistic carbon sites described as Lennard-Jones spheres ($\varepsilon_{CC}/k = 28K$ and $\sigma_{CC} = 3.40 Å$ [24, 40]) in the $xy-$plane, and corresponding to a 10% in-plane biaxial strained condition of the original graphene plates characterized by an adjacent carbon-carbon distance of $1.42 Å$, where these dimensions are always smaller than the $(\mathbb{L}_x, \mathbb{L}_y)-$dimensions of the fluctuating simulation box. Consequently, these aqueous environments were able to behave effectively as grand canonical systems, *i.e.*, by exchanging water molecules with the surroundings to equilibrate the system so that the chemical potential of water is the same everywhere. In fact this simulation scheme allowed us to analyze simultaneously the purely interfacial (*i.e.*, outer left and right) and the confined (*i.e.*, the overlapping between the approaching inner left and right interfacial) microstructures as we changed the interplate distance h. addd here the water-graphene potential info…

here need water-graphene interactions and other simulation details

IV. DISCUSSION OF RESULTS

In order to evaluate the accuracy of the superposition approximations, Eqns. (7) and (8), for the axial water distribution functions under confinement, we compared the actual distribution functions for the water under the "*ff*" graphene plate confinement against the corresponding predicted profiles according to the geometric superposition as illustrated in Figures 3-5 (and Figures S1-S3 in the Supporting Information document) for the interplate distance range $8 \le h(Å) \le 28$. This comparison provides a strong support of the validity of Eqn. (7) as an accurate representation of the density profiles of confined water between flat graphene plates for $h \gtrsim 10 Å$. For interplate distances $h < 10 Å$, Figures 3-4, the geometric superposition becomes less accurate resulting from the packing frustration [73] because the confined space between graphene plates cannot accommodate an integer number of adsorbed water layers, typically at interplate flat-flat

distances similar to the fluid's molecular size, as the left- and right-adsorbed water layers overlap.

Note that the accuracy of the geometric superposition approximation is clearly preserved with changes of temperature and pressure as clearly illustrated in Figures S4-S5, in the Supporting Information document, where we compare the actual distributions for the oxygen and hydrogen water sites against the predicted geometric profiles for $T = 298K$ and $P = 100bar$ as well as $T = 318K$ and $P = 1bar$ for the representative interplate distance $h = 20\text{Å}$. Moreover, as illustrated in Figure S6 of the Supporting Information document, we summarize the $T - P$ effects on the predicted site-density profiles, the evolution of the confined water structure is the one expected, *i.e.*, a small but noticeable increase of the water adsorption under an isothermal compression, and a clear decrease of the water adsorption under an isobaric temperature increase [28, 74].

In contrast to the predicted behavior of the geometric superposition, Figures 3-5 complemented by Figures S1-S3, the arithmetic superposition representation provides unphysical axial distribution profiles for distances $h \lesssim 10\text{Å}$, *i.e.*, negative, positive, and finite correlations within the solid-fluid excluded core distances (volumes) as illustrated in Figures 6-7. Yet, for $h > 10\text{Å}$ the arithmetic superposition representation becomes as accurate as the corresponding geometric one (compare Figures 5 and 8), despite the significant difference between the two approximations as discussed in section II.

Given the outcome from the analysis of overlapping interfacial structures for identical (in registry) "*ff*" graphene surfaces (Figure 2a), it appears enlightening to test the above superposition schemes, *i.e.*, Eqns. (5) and (7), for either pairs of corrugated (Figure 2d-e) or dissimilar surfaces such as the combination of flat and corrugated graphene plates (Figure 2b-c). For this task we have performed additional molecular simulations of the previous systems, now comprising an unstrained flat graphene surface paired to a corrugated plate with dimensions $L_x = 17.44\text{Å}$ by $L_y = 18.44\text{Å}$, with the corrugation function described previously [25], *i.e.,*

$$\delta z_i(x_i, y_i) = a_o \cos\left[2\pi\left(x_i - x_l\right)/\left(x_u - x_l\right)\right]\cos\left[2\pi\left(y_i - y_l\right)/\left(y_u - y_l\right)\right] \qquad (9)$$

positive [negative]

where $\delta z_i(x_i, y_i) > 0$ [$\delta z_i(x_i, y_i) < 0$] describes the "p" ["n"] perturbation of the location of the $z-$coordinate of the $i-$carbon atom located at $z_{right}(x_i, y_i)$ in the original flat graphene surface "f". This corrugation is characterized by the amplitude $a_o = 1.0\,\AA$, while $(x_u - x_l) = L_x$ and $(y_u - y_l) = L_y$ describe the upper most (u) and lowest (l) location of a carbon site in the $xy-$plane (see Figure 2).

According to this corrugation pattern we built four special slit-pore configurations, *i.e.*,

$$\left.\begin{aligned} z_i^{left}(x_i, y_i) &= z_{left} \\ z_i^{right}(x_i, y_i) &= z_{right} + \delta z_i(x_i, y_i) \end{aligned}\right\} \text{"}fp\text{" configuration} \qquad (10)$$

where "*fp*" stands for flat-positive $\delta z_i(\cdots)$, as illustrated in Figure 2b,

$$\left.\begin{aligned} z_i^{left}(x_i, y_i) &= z_{left} \\ z_i^{right}(x_i, y_i) &= z_{right} - \delta z_i(x_i, y_i) \end{aligned}\right\} \text{"}fn\text{" configuration} \qquad (11)$$

where "*fn*" represents the flat-negative $\delta z_i(\cdots)$, as illustrated in Figure 2c,

$$\left.\begin{aligned} z_i^{left}(x_i, y_i) &= z_{left} - \delta z_i(x_i, y_i) \\ z_i^{right}(x_i, y_i) &= z_{right} + \delta z_i(x_i, y_i) \end{aligned}\right\} \text{"}np\text{" configuration} \qquad (12)$$

where "*np*" stands for negative and positive $\delta z_i(\cdots)$, as illustrated in Figure 2d,

$$\left.\begin{aligned} z_i^{left}(x_i, y_i) &= z_{left} + \delta z_i(x_i, y_i) \\ z_i^{right}(x_i, y_i) &= z_{right} + \delta z_i(x_i, y_i) \end{aligned}\right\} \text{"}pp\text{" configuration} \qquad (13)$$

where "*pp*" represents the positive and positive $\delta z_i(\cdots)$, as illustrated in Figure 2e. Moreover, in Eqns (10)-(13) z_{left} [z_{righ}] denotes the axial location of the originally left [right] flat graphene surface in the tetragonal simulation box. Note that, strictly speaking, in order to obtain the profiles of the axial distribution functions for the "*fn*" ["*fp*"] according to the Eqns. (6) and (8) we must overlap the outer interfacial structures of the

"*fp*" ["*fn*"] slit pore configuration, *i.e.*, $g_L(z) \equiv g_{fn}(z)$ [$g_L(z) \equiv g_{fp}(z)$] and $g_R(z) \equiv g_{fp}(h-z)$ [$g_R(z) \equiv g_{fn}(h-z)$], because the inner side of the right plate surface in the "*fp*" ["*fn*"] slit pore configuration is the mirror image of its outer side. Interestingly, as illustrated in Figure S7 for $h = 20\text{Å}$, we find that $g_{fn}(z) = g_{fp}(z)$ so that we can assume with confidence that,

$$\begin{aligned} g_L(z) &\equiv g_{fn}(z) = g_{fp}(z) \\ g_R(z) &\equiv g_{fn}(h-z) = g_{fp}(h-z) \end{aligned} \tag{14}$$

Moreover, according to the results in Figures S8-S9, where we plot the comparison between the outer axial density distributions for the left and right plate interfaces involving the "*fp*", "*pp*" and "*np*" configurations at $h = 20\text{Å}$, as well as the unstrained flat and corrugated free-standing plates (*i.e.*, "*ff*" and "*pp*" with $h = 0\text{Å}$), we also have that,

$$\begin{aligned} g_{fn}(z) &= g_{fp}(z) = \rho_{free\text{-}standing}(z) \\ g_{fn}(h-z) &= g_{fp}(h-z) = \rho_{free\text{-}standing}(h-z) \end{aligned} \tag{15}$$

According to the observed behavior, highlighted by Eqns. (14)-(15), it is not surprising to find that the geometric and arithmetic superposition representations are able to describe accurately the inhomogeneous density profiles of water confined between dissimilar graphene surfaces, such as the "*fp*" plate configuration as illustrated in Figure1 9-10 for $h = 20\text{Å}$.

As demonstrated recently by Driskill *et al.* [4] the graphene-water interactions, and consequently, the resulting interfacial structure depends on the nature of the supporting substrate whose effect has been interpreted in terms of wetting transparency or translucency [75-77]. From an experimental perspective, there are no "free-standing" scenarios, but supported graphene plates as typically encountered in any SFA setup. Therefore, we should expect that the resulting inhomogeneous inner density distribution might also depend on the thickness and nature of the solid plate and/or supporting substrate, *i.e.*, as a result of the outer-to-inner plate/support-mediated fluid correlations [78]. For such a case the observations embodied in Eqns. (14)-(15) will obviously not apply.

V. FINAL REMARKS

In this report we have discussed the microstructural evolution underlying the overlapping process between two approaching uncoupled (flat and/or corrugated) graphene-water interfaces and addressed whether the resulting inhomogeneous density profile of the confined water can be described in terms of the original inhomogeneous density profiles near each of the graphene-water interfaces under the same prevailing fixed state conditions of temperature and pressure.

Toward that goal we extracted the axial distribution functions of the water-sites not only for the uncoupled graphene-water interfaces, but also for the corresponding confined environments over the interplate range $8 \le h(\mathring{A}) \le 28$ at ambient conditions, and used those profiles to test the arithmetic and the geometric superposition approximations for the prediction of the axial density distribution of confined water between flat, corrugated, as well as for a combination of flat and corrugated graphene plates.

The analysis of the simulation results in conjunctions with the superposition predictions suggest that both, arithmetic and geometric, representations perform remarkably well for interplate distances larger than that representing the onset of fluid packing frustration, *i.e.*, $h \lesssim 10\mathring{A}$, at which the innermost adsorbed water layer at the right- and left-graphene plates starts overlapping.

ACKNOWLEDGEMENTS

This research was supported as part of the *Fluid Interface Reactions, Structures and Transport* (FIRST) Center, an Energy Frontier Research Center funded by the US Department of Energy, Office of Science, Office of Basic Energy Sciences. The authors wish to acknowledge Peter T. Cummings for posing the question during the monthly FIRST telecom, on April 2014, whose detailed answer led to the research effort discussed in this work.

Supporting Information Available: This document contains additional supporting evidence for the validity of the arithmetic and geometric superposition approximations as illustrated in Figures S1-S9. This information is available free of charge via the Internet at http://pubs.acs.org.

Table of Content-Graphic

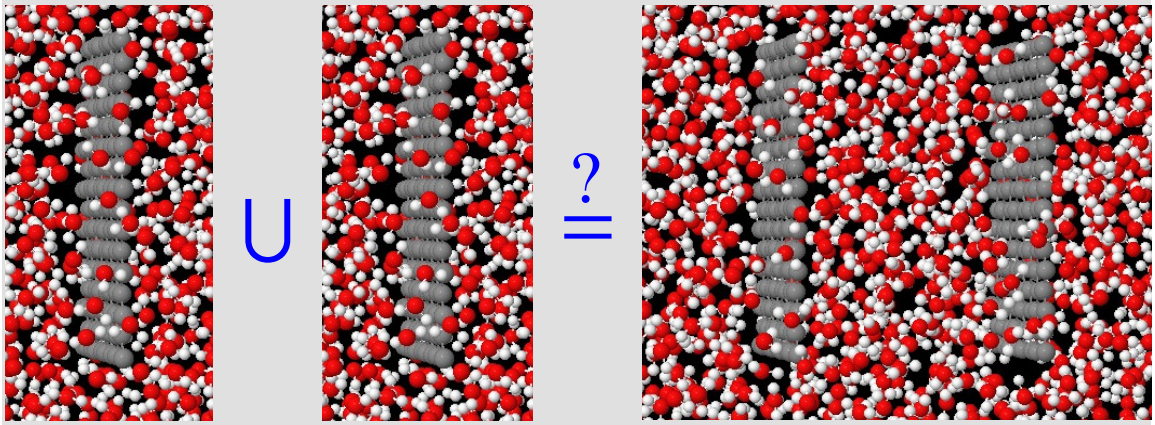

REFERENCES

1. Stillinger, F. H., Structure in Aqueous Solutions of Nonpolar Solutes from the Standpoint of Scaled-Particle Theory. *Journal of Solution Chemistry* **1973**, *2*, 141-158.
2. Lum, K.; Chandler, D.; Weeks, J. D., Hydrophobicity at Small and Large Length Scales. *Journal of Physical Chemistry B* **1999**, *103*, 4570-4577.
3. Maibaum, L.; Chandler, D., A Coarse-Grained Model of Water Confined in a Hydrophobic Tube. *Journal of Physical Chemistry B* **2003**, *107*, 1189-1193.
4. Driskill, J.; Vanzo, D.; Bratko, D.; Luzar, A., Wetting Transparency of Graphene in Water. *The Journal of Chemical Physics* **2014**, *141*, Art. # 18C517.
5. Bellissent-Funel, M. C., Status of Experiments Probing the Dynamics of Water in Confinement. *European Physical Journal E* **2003**, *12*, 83-92.
6. Xu, S.; Simmons, G. C.; Mahadevan, T. S.; Scherer, G. W.; Garofalini, S. H.; Pacheco, C., Transport of Water in Small Pores. *Langmuir* **2009**, *25*, 5084-5090.
7. Zhou, H., et al., Understanding Controls on Interfacial Wetting at Epitaxial Graphene: Experiment and Theory. *Physical Review B* **2012**, *85*.
8. Futamura, R.; Iiyama, T.; Hamasaki, A.; Ozeki, S., Negative Thermal Expansion of Water in Hydrophobic Nanospaces. *Physical Chemistry Chemical Physics* **2012**, *14*, 981-986.
9. Liu, K. H.; Zhang, Y.; Lee, J. J.; Chen, C. C.; Yeh, Y. Q.; Chen, S. H.; Mou, C. Y., Density and Anomalous Thermal Expansion of Deeply Cooled Water Confined in Mesoporous Silica Investigated by Synchrotron X-Ray Diffraction. *Journal of Chemical Physics* **2013**, *139,* Art. # 064502.
10. Diallo, S. O.; Vlcek, L.; Mamontov, E.; Keum, J. K.; Chen, J.; Hayes, J. S.; Chialvo, A. A., Translational Diffusion of Water inside Hydrophobic Carbon Micropores Studied by Neutron Spectroscopy and Molecular Dynamics Simulation. *Physical Review E* **2015**, *91*, 022124.
11. Werder, T.; Walther, J. H.; Jaffe, R. L.; Halicioglu, T.; Koumoutsakos, P., On the Water-Carbon Interaction for Use in Molecular Dynamics Simulations of Graphite and Carbon Nanotubes. *Journal of Physical Chemistry B* **2003**, *107*, 1345-1352.
12. Zangi, R.; Mark, A. E., Electrofreezing of Confined Water. *Journal of Chemical Physics* **2004**, *120*, 7123-7130.
13. Pertsin, A.; Grunze, M., Water-Graphite Interaction and Behavior of Water near the Graphite Surface. *Journal of Physical Chemistry B* **2004**, *108*, 1357-1364.
14. Choudhury, N.; Pettitt, B. M., On the Mechanism of Hydrophobic Association of Nanoscopic Solutes. *Journal of the American Chemical Society* **2005**, *127*, 3556-3567.
15. Yang, X. N.; Yue, X. P., Adsorption and Structure of Lennard-Jones Model Fluid in Slit-Like Amorphous Silica Nanopores. *Colloids and Surfaces a-Physicochemical and Engineering Aspects* **2007**, *301*, 166-173.
16. Cicero, G.; Grossman, J. C.; Schwegler, E.; Gygi, F.; Galli, G., Water Confined in Nanotubes and between Graphene Sheets: A First Principle Study. *Journal of the American Chemical Society* **2008**, *130*, 1871-1878.
17. Eun, C.; Berkowitz, M. L., Origin of the Hydration Force: Water-Mediated Interaction between Two Hydrophilic Plates. *Journal of Physical Chemistry B* **2009**, *113*, 13222-13228.

18. Gordillo, M. C.; Marti, J., Water on Graphene Surfaces. *Journal of Physics-Condensed Matter* **2010**, *22*.
19. Striolo, A., From Interfacial Water to Macroscopic Observables: A Review. *Adsorption Science & Technology* **2011**, *29*, 211-258.
20. Zangi, R., Driving Force for Hydrophobic Interaction at Different Length Scales. *The Journal of Physical Chemistry B* **2011**, *115*, 2303-2311.
21. Eun, C.; Berkowitz, M. L., Molecular Dynamics Simulation Study of the Water-Mediated Interaction between Zwitterionic and Charged Surfaces. *Journal of Chemical Physics* **2012**, *136,* Art. # 024501.
22. Giovambattista, N.; Rossky, P. J.; Debenedetti, P. G., Computational Studies of Pressure, Temperature, and Surface Effects on the Structure and Thermodynamics of Confined Water. In *Annual Review of Physical Chemistry, Vol 63*, Johnson, M. A.; Martinez, T. J., Eds. 2012; Vol. 63, pp 179-200.
23. Ho, T. A.; Papavassiliou, D. V.; Lee, L. L.; Striolo, A., Liquid Water Can Slip on a Hydrophilic Surface. *Proceedings of the National Academy of Sciences of the United States of America* **2011**, *108*, 16170-16175.
24. Chialvo, A. A.; Cummings, P. T., Aqua Ions-Graphene Interfacial and Confinement Behavior: Insights from Isobaric-Isothermal Molecular Dynamics. *The Journal of Physical Chemistry A* **2011**, *115*, 5918-5927.
25. Chialvo, A. A.; Vlcek, L.; Cummings, P. T., Surface Corrugation Effects on the Water–Graphene Interfacial and Confinement Behavior. *The Journal of Physical Chemistry C* **2013**, *117*, 23875-23886.
26. Ball, P., Chemical Physics: How to Keep Dry in Water. *Nature* **2003**, *423*, 25-26.
27. Zangi, R., Water Confined to a Slab Geometry: A Review of Recent Computer Simulation Studies. *Journal of Physics-Condensed Matter* **2004**, *16*, S5371-S5388.
28. Giovambattista, N.; Rossky, P. J.; Debenedetti, P. G., Effect of Pressure on the Phase Behavior and Structure of Water Confined between Nanoscale Hydrophobic and Hydrophilic Plates. *Physical Review E* **2006**, *73*.
29. Vanzo, D.; Bratko, D.; Luzar, A., Dynamic Control of Nanopore Wetting in Water and Saline Solutions under an Electric Field. *The Journal of Physical Chemistry B* **2015**, *119*, 8890-8899.
30. Diallo, S. O., Pore-Size Dependence and Characteristics of Water Diffusion in Slitlike Micropores. *Physical Review E* **2015**, *92*.
31. Perret, E.; Nygard, K.; Satapathy, D. K.; Balmer, T. E.; Bunk, O.; Heuberger, M.; van der Veen, J. F., X-Ray Reflectivity Reveals Equilibrium Density Profile of Molecular Liquid under Nanometre Confinement. *Epl* **2009**, *88*.
32. Argyris, D.; Ho, T. A.; Cole, D. R.; Striolo, A., Molecular Dynamics Studies of Interfacial Water at the Alumina Surface. *Journal of Physical Chemistry C* **2011**, *115*, 2038-2046.
33. Nygard, K.; Konovalov, O., Decay of Interfacial Fluid Ordering Probed by X-Ray Reflectivity. *Soft Matter* **2012**, *8*, 5180-5186.
34. Phan, A.; Ho, T. A.; Cole, D. R.; Striolo, A., Molecular Structure and Dynamics in Thin Water Films at Metal Oxide Surfaces: Magnesium, Aluminum, and Silicon Oxide Surfaces. *Journal of Physical Chemistry C* **2012**, *116*, 15962-15973.

35. Chodankar, S.; Perret, E.; Nygard, K.; Bunk, O.; Satapathy, D. K.; Marzal, R. M. E.; Balmer, T. E.; Heuberger, M.; van der Veen, J. F., Density Profile of Water in Nanoslit. *Epl* **2012**, *99*.
36. Fenter, P.; Lee, S. S., Hydration Layer Structure at Solid–Water Interfaces. *MRS Bulletin* **2014**, *39*, 1056-1061.
37. Kroutil, O.; Chval, Z.; Skelton, A. A.; Předota, M., Computer Simulations of Quartz (101)–Water Interface over a Range of Ph Values. *The Journal of Physical Chemistry C* **2015**, *119*, 9274-9286.
38. Chialvo, A. A.; Vlcek, L.; Cole, D. R., Aqueous Co2 Solutions at Silica Surfaces and within Nanopore Environments. Insights from Isobaric-Isothermal Molecular Dynamics. *Journal of Physical Chemistry C* **2012**, *116*, 13904-13916.
39. Chialvo, A. A.; Vlcek, L.; Cummings, P. T., Surface Strain Effects on the Water–Graphene Interfacial and Confinement Behavior. *The Journal of Physical Chemistry C* **2014**, *118*, 19701-19711.
40. Chialvo, A. A.; Vlcek, L.; Cummings, P. T., Compounding Effects of Fluid Confinement and Surface Strain on the Wet-Dry Transition, Thermodynamic Response, and Dynamics of Water-Graphene Systems. *Molecular Physics* **2015**, *113*, 1033-1042.
41. Giovambattista, N.; Debenedetti, P. G.; Rossky, P. J., Effect of Surface Polarity on Water Contact Angle and Interfacial Hydration Structure. *Journal of Physical Chemistry B* **2007**, *111*, 9581-9587.
42. Vlcek, L.; Cummings, P. T., Adsorption of Water on Tio2 and Sno2 Surfaces: Molecular Dynamics Study. *Collection of Czechoslovak Chemical Communications* **2008**, *73*, 575-589.
43. Ohler, B.; Langel, W., Molecular Dynamics Simulations on the Interface between Titanium Dioxide and Water Droplets: A New Model for the Contact Angle. *Journal of Physical Chemistry C* **2009**, *113*, 10189-10197.
44. Chai, J. C.; Liu, S. Y.; Yang, X. N., Molecular Dynamics Simulation of Wetting on Modified Amorphous Silica Surface. *Applied Surface Science* **2009**, *255*, 9078-9084.
45. Choudhury, N., Dynamics of Water at the Nanoscale Hydrophobic Confinement. *Journal of Chemical Physics* **2010**, *132*.
46. Solc, R.; Gerzabek, M. H.; Lischka, H.; Tunega, D., Wettability of Kaolinite (001) Surfaces - Molecular Dynamic Study. *Geoderma* **2011**, *169*, 47-54.
47. Li, H.; Zeng, X. C., Wetting and Interfacial Properties of Water Nanodroplets in Contact with Graphene and Monolayer Boron-Nitride Sheets. *ACS Nano* **2012**, *6*, 2401-2409.
48. Joly, L.; Ybert, C.; Bocquet, L., Probing the Nanohydrodynamics at Liquid-Solid Interfaces Using Thermal Motion. *Physical Review Letters* **2006**, *96*.
49. Choi, C. H.; Kim, C. J., Large Slip of Aqueous Liquid Flow over a Nanoengineered Superhydrophobic Surface. *Physical Review Letters* **2006**, *96*.
50. Dorrer, C.; Ruhe, J., Some Thoughts on Superhydrophobic Wetting. *Soft Matter* **2009**, *5*, 51-61.
51. Wong, T. S.; Ho, C. M., Dependence of Macroscopic Wetting on Nanoscopic Surface Textures. *Langmuir* **2009**, *25*, 12851-12854.

52. Daub, C. D.; Wang, J. H.; Kudesia, S.; Bratko, D.; Luzar, A., The Influence of Molecular-Scale Roughness on the Surface Spreading of an Aqueous Nanodrop. *Faraday Discussions* **2010**, *146*, 67-77.
53. Yan, Y. Y.; Gao, N.; Barthlott, W., Mimicking Natural Superhydrophobic Surfaces and Grasping the Wetting Process: A Review on Recent Progress in Preparing Superhydrophobic Surfaces. *Advances in Colloid and Interface Science* **2011**, *169*, 80-105.
54. Xu, W.; Choi, C.-H., From Sticky to Slippery Droplets: Dynamics of Contact Line Depinning on Superhydrophobic Surfaces. *Physical Review Letters* **2012**, *109*.
55. Nygård, K.; Satapathy, D. K.; Buitenhuis, J.; Perret, E.; Bunk, O.; David, C.; Veen, J. F. v. d., Confinement-Induced Orientational Alignment of Quasi-2d Fluids. *EPL (Europhysics Letters)* **2009**, *86*, 66001.
56. Perret, E.; Nygard, K.; Satapathy, D. K.; Balmer, T. E.; Bunk, O.; Heuberger, M.; van der Veen, J. F., X-Ray Reflectivity Theory for Determining the Density Profile of a Liquid under Nanometre Confinement. *Journal of Synchrotron Radiation* **2010**, *17*, 465-472.
57. Nakano, S.; Mizukami, M.; Ohta, N.; Yagi, N.; Hatta, I.; Kurihara, K., Structural Change in Smectic Liquid Crystal Nanofilm under Molecular-Scale Confinement Measured by Synchrotron X-Ray Diffraction. *Japanese Journal of Applied Physics* **2013**, *52*.
58. Lippmann, M.; Ehnes, A.; Seeck, O. H., An X-Ray Setup to Investigate the Atomic Order of Confined Liquids in Slit Geometry. *Review of Scientific Instruments* **2014**, *85*, 015106.
59. Amano, K.-i.; Takahashi, O., Simple Transform Methods of a Force Curve Obtained by Surface Force Apparatus to the Density Distribution of a Liquid near a Surface. *Physica a-Statistical Mechanics and Its Applications* **2015**, *425*, 79-89.
60. Amano, K.-I.; Tanaka, E.; Kobayashi, K.; Onishi, H.; Nishi, N.; Sakka, T., Force Measurement Reveals Structure of a Confined Liquid: Observation of the Impenetrable Space. *Surface Science* **2015**, *641*, 242-246.
61. Evans, R.; Marconi, U. M. B., Phase-Equilibria and Solvation Forces for Fluids Confined between Parallel Walls. *Journal of Chemical Physics* **1987**, *86*, 7138-7148.
62. Evans, R., Nature of the Liquid-Vapor Interface and Other Topics in the Statistical-Mechanics of Nonuniform, Classical Fluids. *Advances in Physics* **1979**, *28*, 143-200.
63. Powles, J. G.; Holtz, B.; Evans, W. A. B., New Method for Determining the Chemical-Potential for Condensed Matter at High-Density. *Journal of Chemical Physics* **1994**, *101*, 7804-7810.
64. Heller, D. F.; Harris, R. A.; Gelbart, W. M., Density Functional Formulation of Collisional Polarizabilities - Application to Homonuclear Noble-Gas Diatoms. *Journal of Chemical Physics* **1975**, *62*, 1947-1953.
65. Harris, R. A., Density Functional Theory of Vanderwaals Forces. *Chemical Physics Letters* **1975**, *33*, 495-498.
66. Gombás, P., Über Eine Vereinfachte Methode Des Self-Consistent Field Für Atome. *Theoretica chimica acta* **1966**, *5*, 112-126.
67. Gaydaenko, V. I.; Nikulin, V. K., Born-Mayer Interatomic Potential for Atoms with Z=2 to Z=36. *Chemical Physics Letters* **1970**, *7*, 360-362.

68. Kirkwood, J. G., Statistical Mechanics of Fluid Mixtures. *Journal of Chemical Physics* **1935**, *3*, 300-313.
69. Verwey, E. J. W.; Overbeek, J. T. G., *Theory of the Stability of Lyophobic Colloids. The Interaction of Particles Having and Electric Double Layer*; Elsevier Publishing Co.: Amsterdam 1948.
70. Berendsen, H. J. C.; Grigera, J. R.; Straatsma, T. P., The Missing Term in Effective Pair Potentials. *Journal of Physical Chemistry* **1987**, *91*, 6269-6271.
71. Nose, S., An Improved Symplectic Integrator for Nose-Poincare Thermostat. *Journal of the Physical Society of Japan* **2001**, *70*, 75-77.
72. Okumura, H.; Itoh, S. G.; Okamoto, Y., Explicit Symplectic Integrators of Molecular Dynamics Algorithms for Rigid-Body Molecules in the Canonical, Isobaric-Isothermal, and Related Ensembles. *Journal of Chemical Physics* **2007**, *126*.
73. Yu, B.; Sun, P. C.; Chen, T. H.; Jin, Q. H.; Ding, D. T.; Li, B. H.; Shi, A. C., Confinement-Induced Novel Morphologies of Block Copolymers. *Physical Review Letters* **2006**, *96*.
74. Giovambattista, N.; Rossky, P. J.; Debenedetti, P. G., Effect of Temperature on the Structure and Phase Behavior of Water Confined by Hydrophobic, Hydrophilic, and Heterogeneous Surfaces. *The Journal of Physical Chemistry B* **2009**, *113*, 13723-13734.
75. Shih, C. J.; Strano, M. S.; Blankschtein, D., Wetting Translucency of Graphene. *Nature Materials* **2013**, *12*, 866-869.
76. Raj, R.; Maroo, S. C.; Wang, E. N., Wettability of Graphene. *Nano Letters* **2013**, *13*, 1509-1515.
77. Li, Z., et al., Effect of Airborne Contaminants on the Wettability of Supported Graphene and Graphite. *Nat Mater* **2013**, *12*, 925-931.
78. Olivares, W.; Degreve, L.; Villegas, J. C.; Lozada-Cassou, M., Liquid Correlation across the Walls in a Slit Pore: Effect on the Wetting and Drying Transition. *Physical Review E* **2002**, *65*.

FIGURE CAPTIONS

Figure 1: Schematic representation of the formation of a confined fluid as a result of approaching solid-fluid interfacial regions, where $\rho_L(z) \equiv \rho_{free\text{-}standing}(z)$ and $\rho_R(z) \equiv \rho_{free\text{-}standing}(h-z)$.

Figure 2: Schematic representation of the three types of slit pores: (a) in registry flat plate-flat plate configuration, (b) flat plate plus a "*p*"-corrugated plate (*aka* "*fp*") configuration, (c) flat plate plus a "*n*"-corrugated plate (*aka* "*fn*"), (d) an "*n*"-corrugated plate plus a "*p*"-corrugated plate (*aka* "*np*") configuration, and (e) two "in registry" "*p*"-corrugated plates (*aka* "*pp*") configuration, with preserving confined volume at a fixed interplate distance h.

Figure 3: Comparison of water-site axial distribution functions between the geometric superposition (*i.e.*, left-right overlap) outcome and the actual behavior for confined water in a strained "*ff*" graphene plate configuration at an interplate distance $h = 8\,\text{Å}$ at ambient conditions.

Figure 4: Comparison of water-site axial distribution functions between the geometric superposition (*i.e.*, left-right overlap) outcome and the actual behavior for confined water in a strained "*ff*" graphene plate configuration at an interplate distance $h = 10\,\text{Å}$ at ambient conditions.

Figure 5: Comparison of water-site axial distribution functions between the geometric superposition (*i.e.*, left-right overlap) outcome and the actual behavior for confined water in a strained "*ff*" graphene plate configuration at an interplate distance $h = 20\,\text{Å}$ at ambient conditions.

Figure 6: Comparison of water-site axial distribution functions between the arithmetic and the geometric superposition outcomes for confined water in a strained "*ff*" graphene plate configuration at an interplate distance $h = 8\,\text{Å}$ at ambient conditions.

Figure 7: Comparison of water-site axial distribution functions between the arithmetic and the geometric superposition outcomes for confined water in an "*ff*"

graphene plate configuration at an interplate distance $h = 10\,\mathring{A}$ at ambient conditions.

Figure 8: Comparison of water-site axial distribution functions between the arithmetic superposition outcome and the actual behavior for confined water in a strained "*ff*" graphene plate configuration at an interplate distance $h = 20\,\mathring{A}$ at ambient conditions.

Figure 9: Comparison of water-site axial distribution functions between the geometric superposition outcome and the actual behavior for confined water in an "*fp*" graphene plate configuration at an interplate distance $h = 20\,\mathring{A}$ at ambient conditions.

Figure 10: Comparison of water-site axial distribution functions between the geometric and arithmetic superposition outcomes for confined water in an "*fp*" graphene plate configuration at an interplate distance $h = 20\,\mathring{A}$ at ambient conditions.

Figure 1

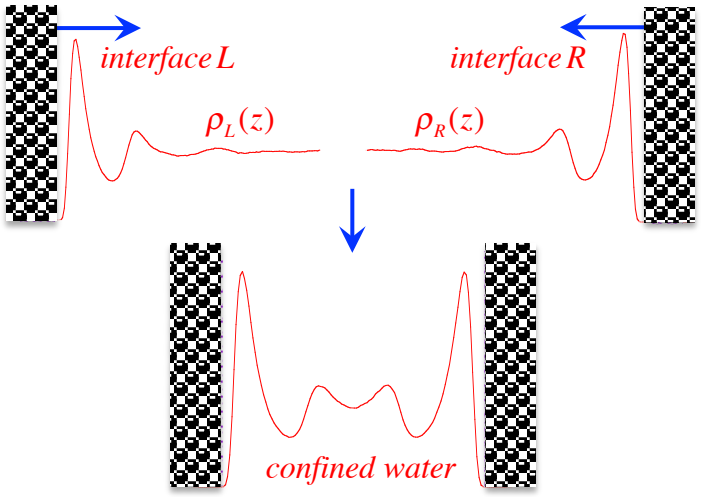
interface L
interface R
$\rho_L(z)$
$\rho_R(z)$
confined water
$\rho_L(z) \cup \rho_R(z) \xrightarrow{?} \rho_{confinement}(z)$

Figure 2

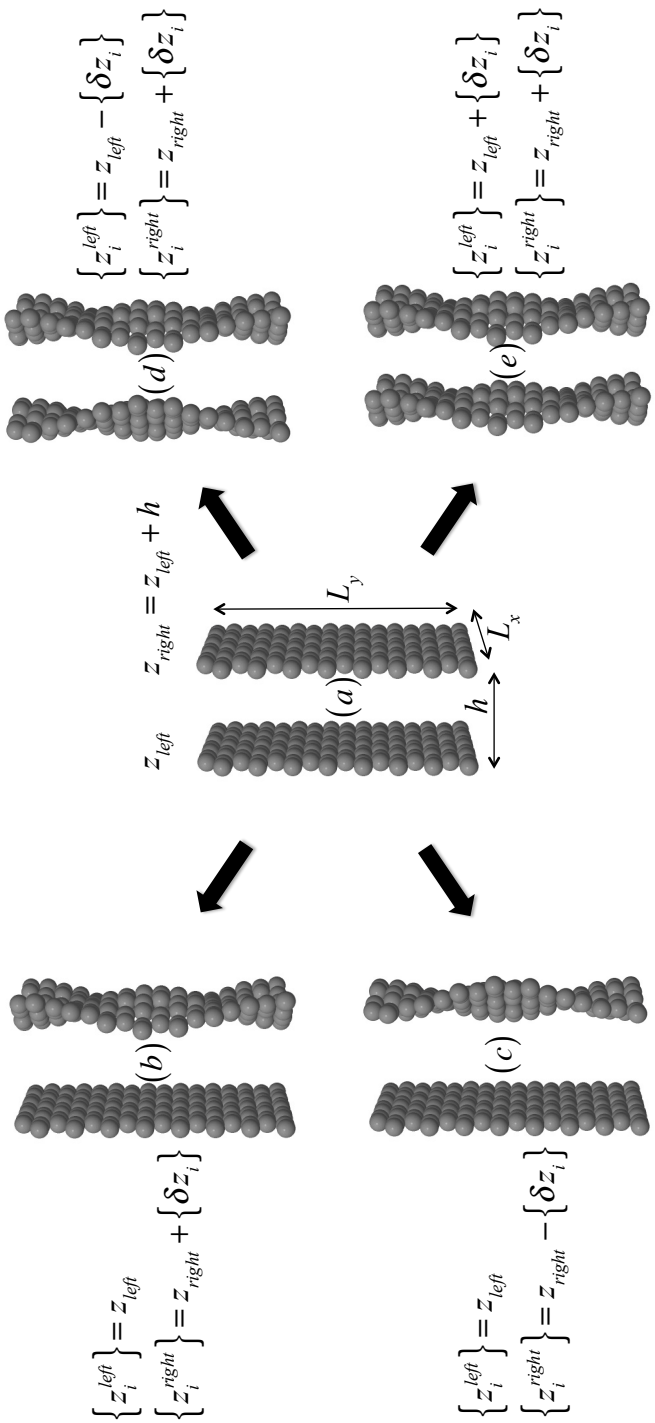
$\{z_i^{left}\} = z_{left} - \{\delta z_i\}$
$\{z_i^{right}\} = z_{right} + \{\delta z_i\}$
(d)
$\{z_i^{left}\} = z_{left} + \{\delta z_i\}$
$\{z_i^{right}\} = z_{right} + \{\delta z_i\}$
(e)
$z_{right} = z_{left} + h$
L_y
L_x
z_{left}
(a)
h
(b)
$\{z_i^{left}\} = z_{left}$
$\{z_i^{right}\} = z_{right} + \{\delta z_i\}$
(c)
$\{z_i^{left}\} = z_{left}$
$\{z_i^{right}\} = z_{right} - \{\delta z_i\}$

Figure 3

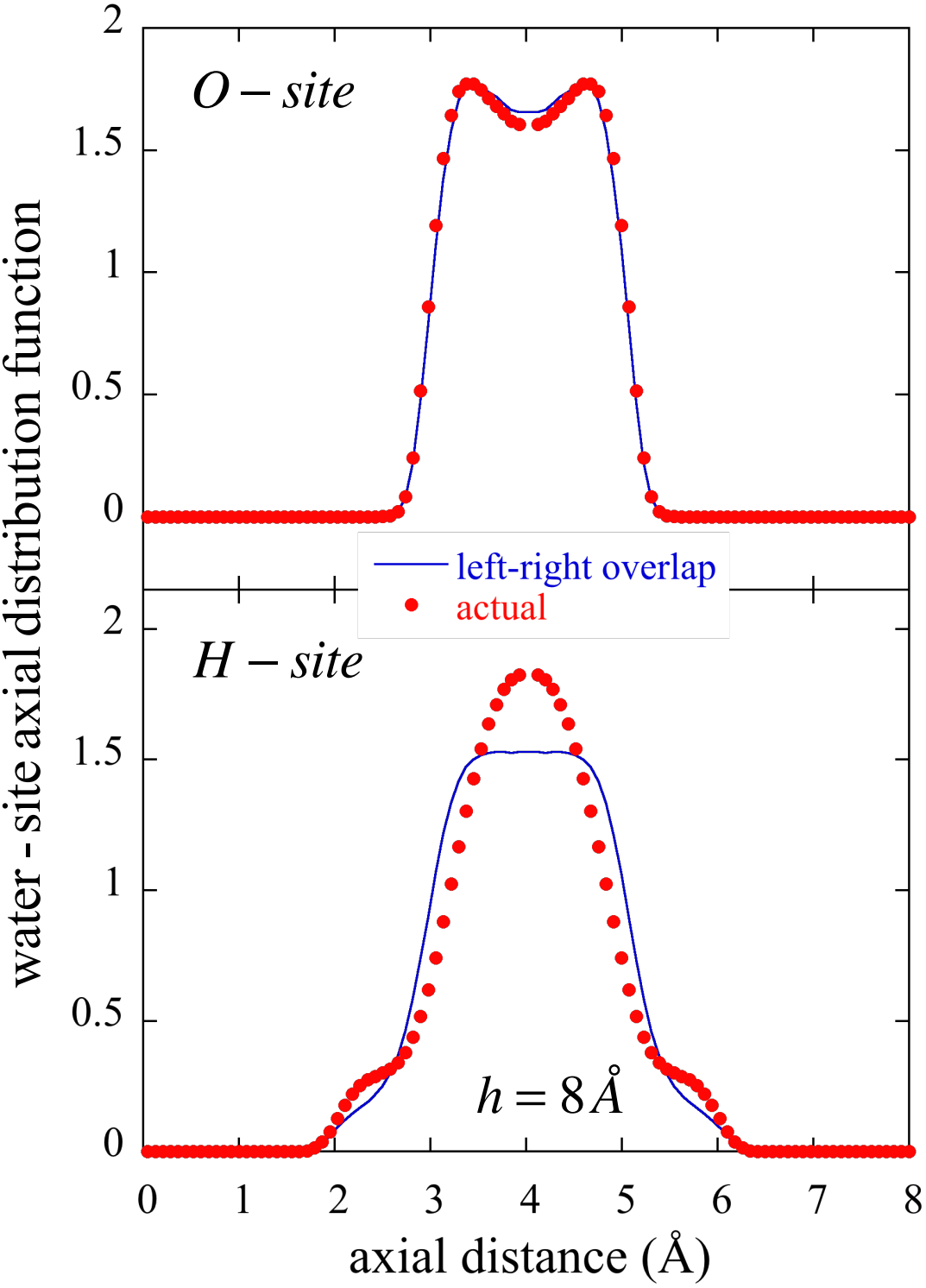
O – site
H – site
left-right overlap
actual
h = 8 Å
water - site axial distribution function
axial distance (Å)
0
0.5
1
1.5
2
0
1
2
3
4
5
6
7
8

Figure 4

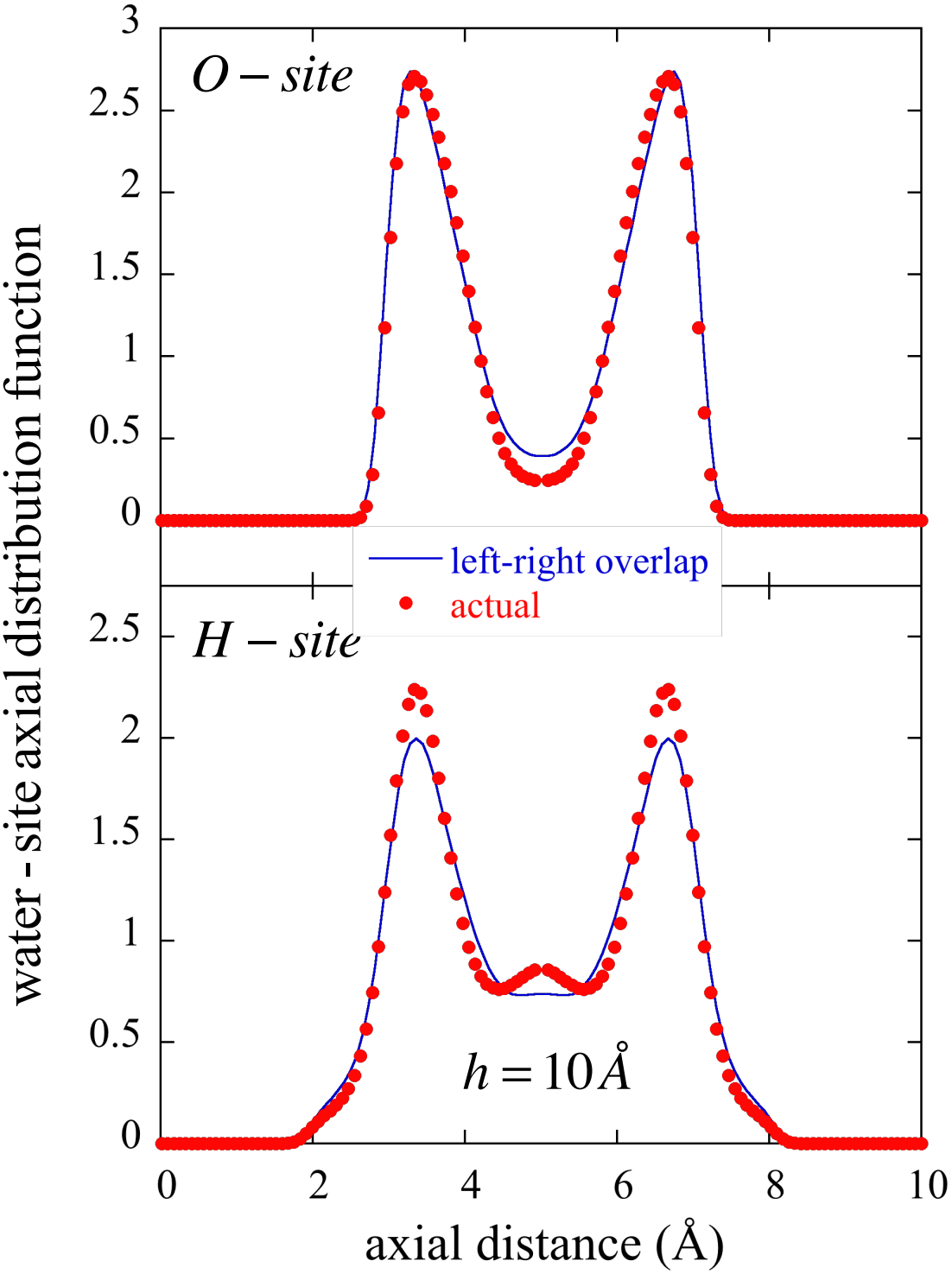
O – site
H – site
left-right overlap
actual
h = 10 Å
water - site axial distribution function
axial distance (Å)
0
0.5
1
1.5
2
2.5
3
0
2
4
6
8
10

Figure 5

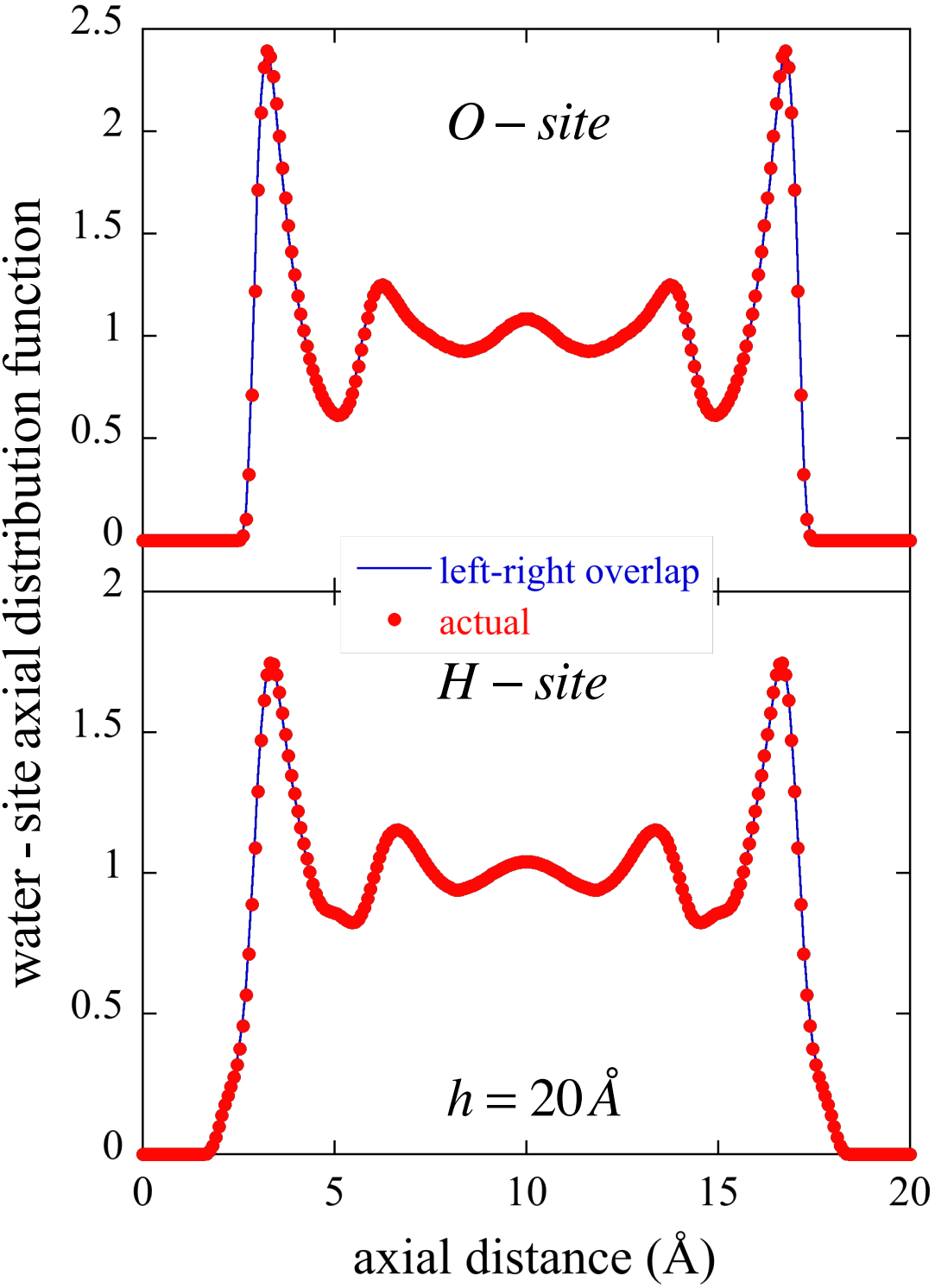
2.5
2
1.5
1
0.5
0
O – site
left-right overlap
actual
2
1.5
1
0.5
0
H – site
h = 20 Å
0
5
10
15
20
water - site axial distribution function
axial distance (Å)

Figure 6

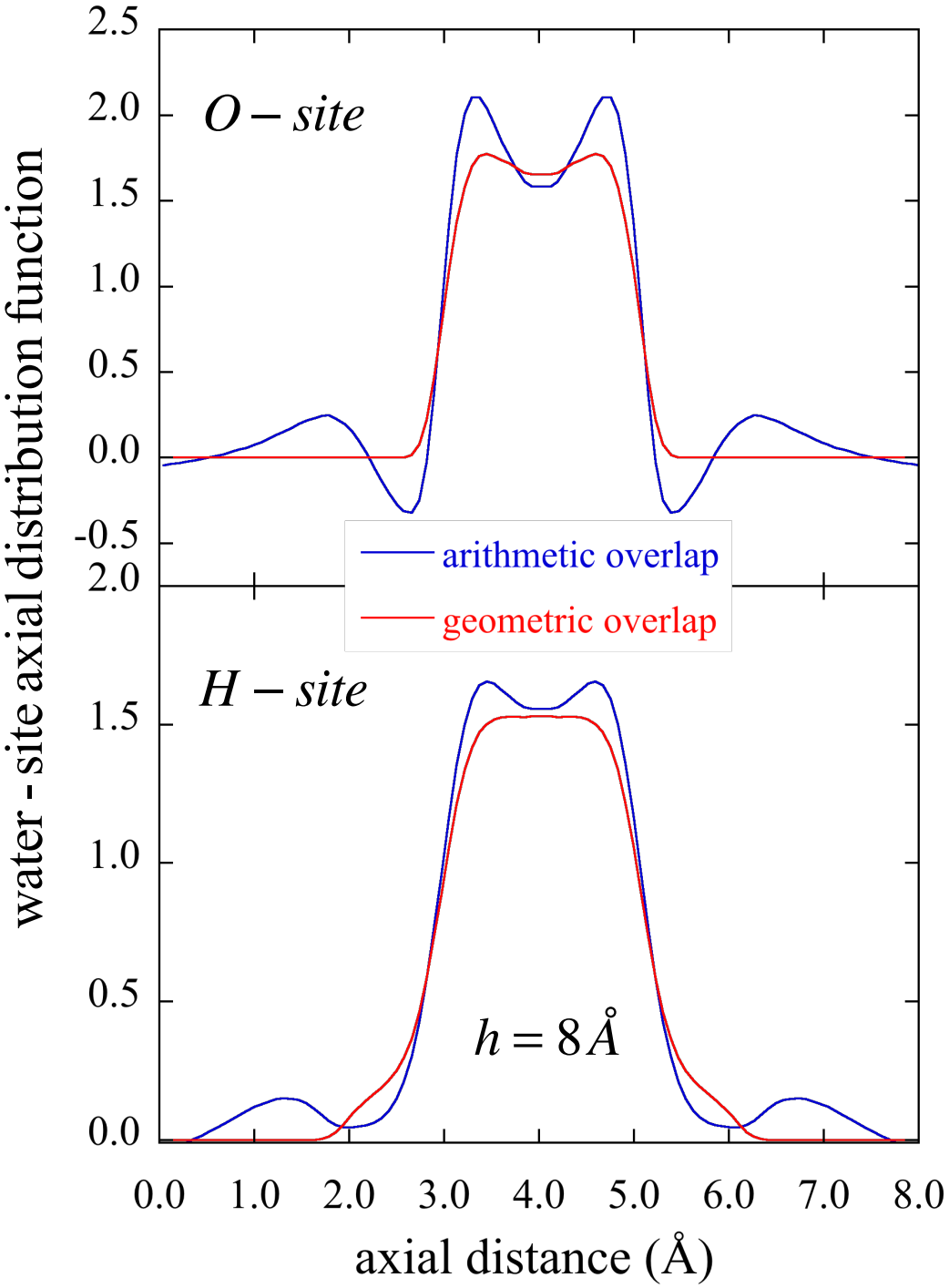
O – site
H – site
arithmetic overlap
geometric overlap
h = 8 Å
water - site axial distribution function
axial distance (Å)
2.5
2.0
1.5
1.0
0.5
0.0
-0.5
0.0
1.0
2.0
3.0
4.0
5.0
6.0
7.0
8.0

Figure 7

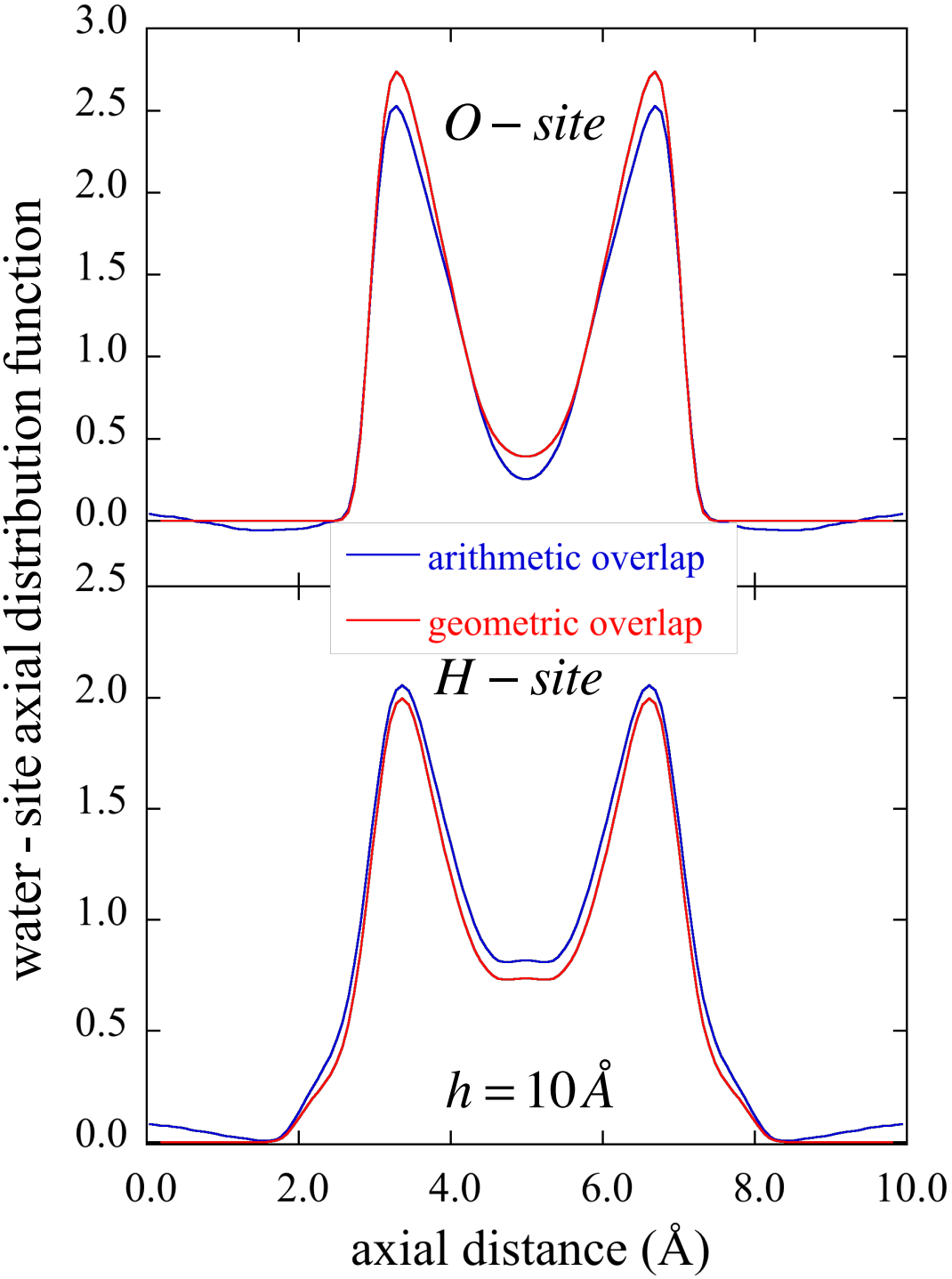
3.0
2.5
2.0
1.5
1.0
0.5
0.0
O – site
arithmetic overlap
geometric overlap
H – site
h = 10 Å
water - site axial distribution function
0.0
2.0
4.0
6.0
8.0
10.0
axial distance (Å)

Figure 8

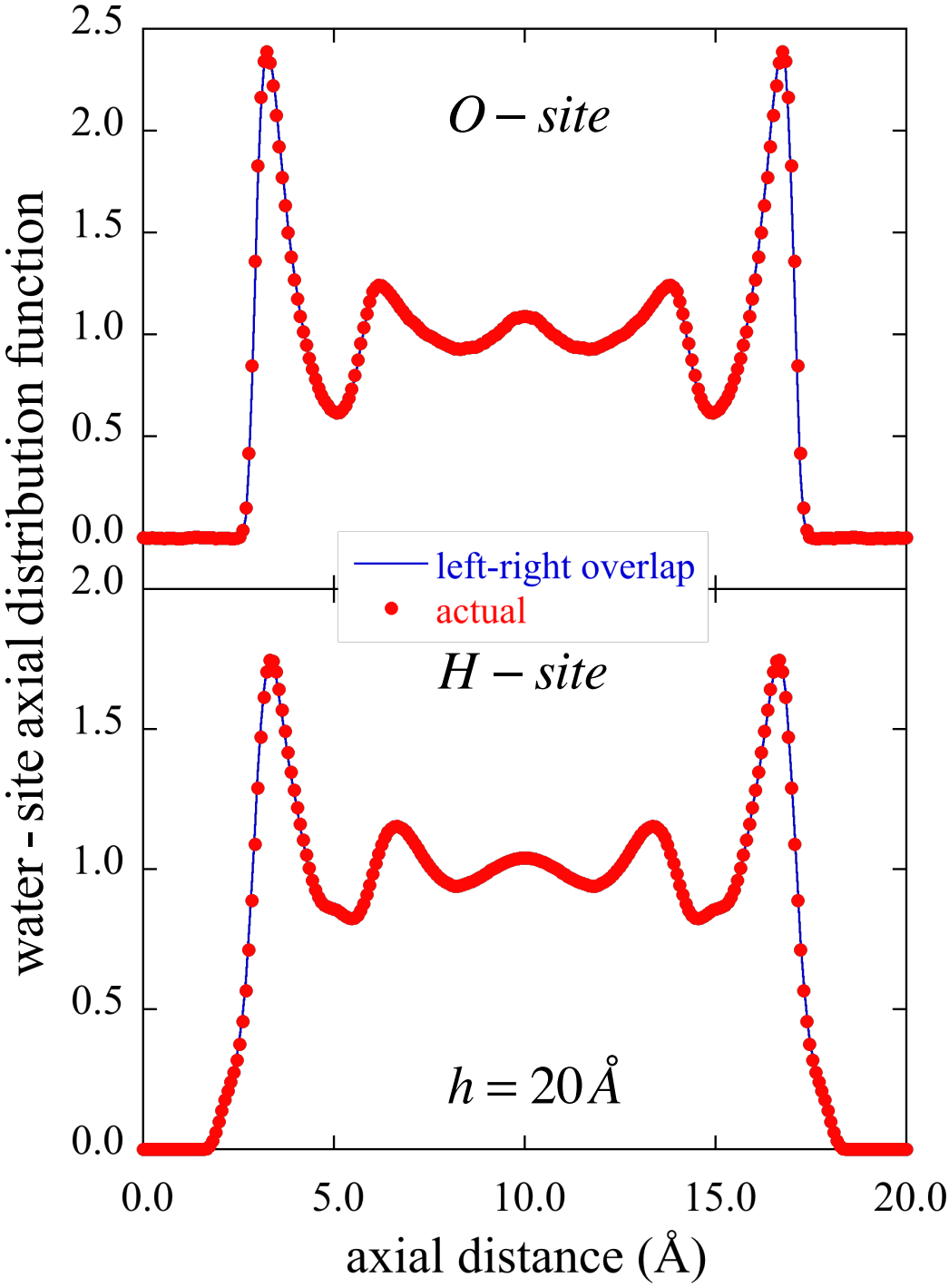
2.5
2.0
1.5
1.0
0.5
0.0
O – site
left-right overlap
actual
H – site
h = 20 Å
water - site axial distribution function
0.0
5.0
10.0
15.0
20.0
axial distance (Å)

Figure 9

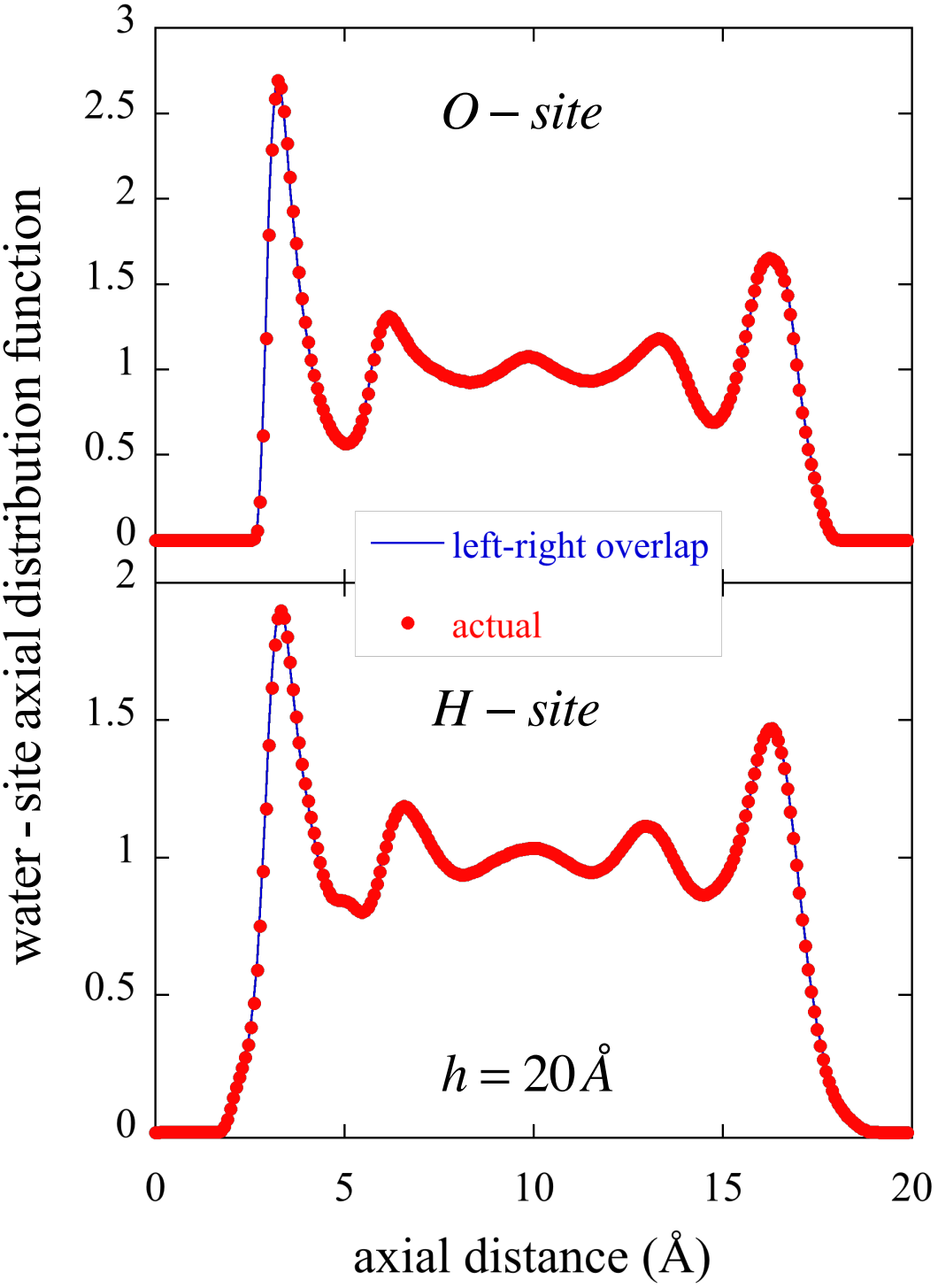
O – site
H – site
left-right overlap
actual
h = 20 Å
water - site axial distribution function
axial distance (Å)
0
0.5
1
1.5
2
2.5
3
5
10
15
20

Figure 10

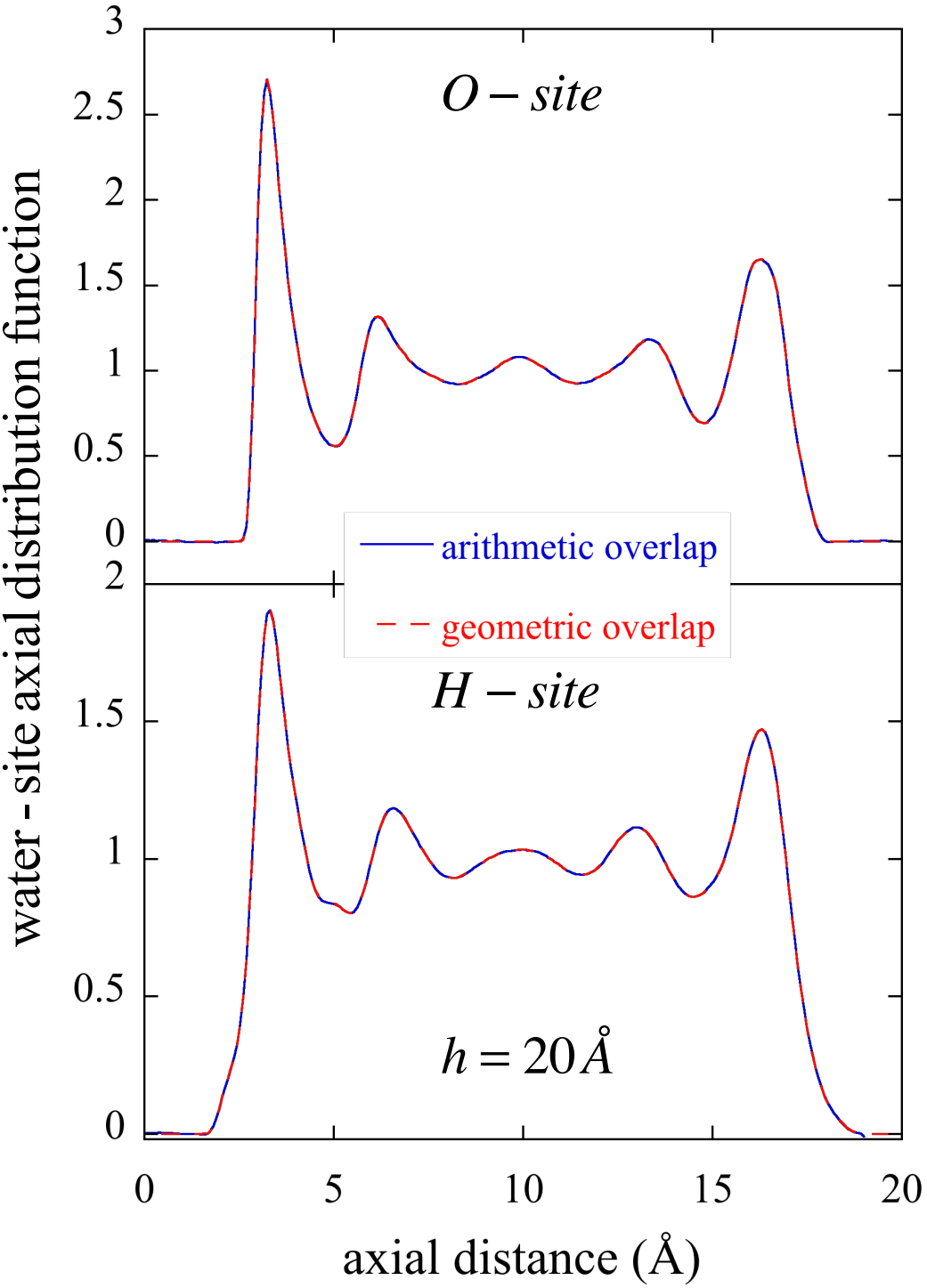
O – site
H – site
arithmetic overlap
geometric overlap
h = 20 Å
water - site axial distribution function
axial distance (Å)
0
0.5
1
1.5
2
2.5
3
0
5
10
15
20